RESEARCH ARTICLE
SOLID EARTH: SEISMOLOGY

Earth and Planetary Physics
10: 512–523, 2026
doi: 10.26464/epp2026049

The triple junction as the preferred nucleation site on the main East Anatolian Fault for the 2023 M_w 7.8 Kahramanmaraş Earthquake: Insights from 3D dynamic rupture simulations

XiuSong Peng[1], ZeYu Lu[1], and Feng Hu[1,2*]

[1]State Key Laboratory of Precision Geodesy, School of Earth and Space Sciences, University of Science and Technology of China, Hefei 230026, China;

[2]Mengcheng National Geophysical Observatory, University of Science and Technology of China, Mengcheng Anhui 233500, China

Key Points:

- The triple junction is the most plausible nucleation site on the main East Anatolian Fault for the 2023 M_w 7.8 Kahramanmaraş Earthquake.
- Rupture initiation at the site 9 km southwest of the triple junction requires additional localized initial stress perturbation.
- The rupture on the Narlı branch fault attains supershear speed but does not approach the P-wave speed.

Citation: Peng, X. S., Lu, Z. Y., and Hu, F. (2026). The triple junction as the preferred nucleation site on the main East Anatolian Fault for the 2023 M_w 7.8 Kahramanmaraş Earthquake: Insights from 3D dynamic rupture simulations. *Earth Planet. Phys.*, *10*(3), 512–523. http://doi.org/10.26464/epp2026049

Abstract: Understanding rupture transfer across fault junctions is critical for interpreting complex multi-fault earthquakes. For the 2023 M_w 7.8 Kahramanmaraş event, we construct three dynamic rupture models constrained by surface fault traces, relocated aftershocks, kinematic slip inversions, near-field strong-motion records, and GPS data to distinguish among potential nucleation sites along the East Anatolian Fault (EAF). Our simulations reveal that although the final slip distributions are insensitive to the precise nucleation point owing to complex fault geometry, the dynamic conditions required for rupture initiation on the EAF differ significantly. Nucleation at the triple junction is facilitated by dynamic Coulomb stress triggering from the Narlı branch fault. Although the supershear rupture velocity is different along the Narlı branch fault of Model 1 and Model 3, both models support nucleation at the triple junction. In contrast, nucleation at 9 km southwest of the triple junction requires artificial stress concentrations, as shown in Model 2. Model 3 shares the same stress concentration along the EAF; however, its near-P-wave supershear speed along the branch fault narrows the Mach cone and directly impedes nucleation to the southwest. All the models show good correspondence with the near-field seismogram and GPS observations. Additionally, we compare the source time functions of the three models with the U.S. Geological Survey result, which imply that the near-P-wave supershear speed along the branch fault is less likely. Our results suggest the triple junction is the most likely nucleation site, and although the 9 km southwest of the triple junction is still possible, it requires highly localized initial stress concentrations.

Keywords: branch fault; rupture nucleation site; dynamic rupture simulation

1. Introduction

On February 6, 2023, a doublet earthquake sequence comprising two major events of moment magnitude M_w 7.8 and M_w 7.6 struck southeastern Türkiye and northern Syria (Melgar et al., 2023; Okuwaki et al., 2023). The sequence occurred within a complex fault system at the triple junction of the Anatolian, Arabian, and African Plates (Figure 1). The first event (M_w 7.8) nucleated at 37.2444°N, 37.0234°E (Melgar et al., 2023) on the Narlı fault, a left-lateral strike-slip branch of the East Anatolian Fault (EAF). Rupture initiated on the Narlı fault, propagated along the branch, and then transferred to the EAF, where it continued bilaterally for ~90 s, producing an ~350-km-long surface rupture (Barbot et al., 2023; Mai PM et al., 2023; Melgar et al., 2023; Okuwaki et al., 2023). Nine hours later, the second event (M_w 7.6) nucleated on the Sürgü–Misis Fault, ~90 km north-northeast of the M_w 7.8 epicenter. This event also ruptured bilaterally, generating an ~150-km-long surface rupture (Jia Z et al., 2023; Xi X et al., 2025). Aftershocks of the doublet are shown in Figure 1. The combined ruptures caused extensive structural damage across 11 major cities in Türkiye and northwestern Syria, resulting in approximately 50,000 fatalities, 100,000 injuries, and direct economic losses exceeding USD 100 billion. The sequence is one of the largest recorded continental strike-slip earthquakes in recent history.

The East Anatolian Fault Zone (EAFZ) is one of the most seismically active regions in Türkiye and the Middle East. Situated at the triple

---

First author: X. S. Peng, pxs0920@mail.ustc.edu.cn
Correspondence to: F. Hu, hufeng07@ustc.edu.cn
Received 25 NOV 2025; Accepted 07 APR 2026.

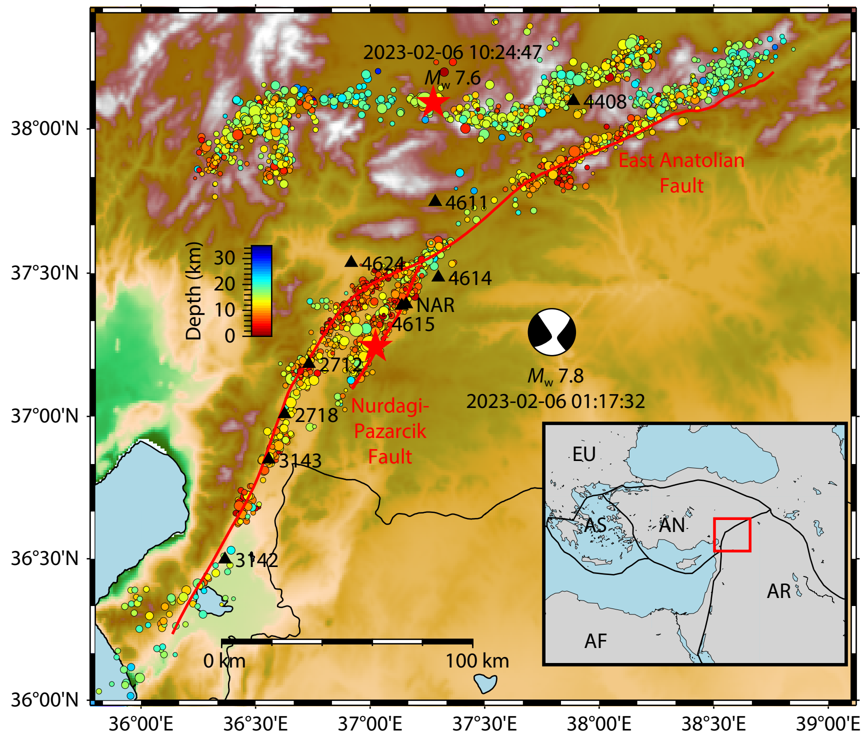

Figure 1. Tectonic setting of the 2023 M_w 7.8 Kahramanmaraş Earthquake. The colored dots represent the aftershock distribution of this earthquake event. The black triangles indicate the distribution of near-field strong ground motion stations; the red pentagram marks the epicenter location. The inset in the lower right corner shows the plate tectonics around the study area, where EU denotes the Eurasian Plate, AS denotes the Aegean Sea, AF denotes the African Plate, AN denotes the Anatolian Plate, and AR denotes the Arabian Plate.

junction of the Anatolian, Arabian, and African Plates, the EAFZ exhibits elevated seismicity driven primarily by interactions between the Arabian and Anatolian Plates (Ambraseys, 1989). Northward indentation of the Arabian Plate induces predominant left-lateral strike-slip displacement along the EAFZ at nearly 10 mm/yr (Reilinger et al., 2006). The EAFZ consists of segmented strike-slip faults with associated bends and branch structures; it has generated multiple historical devastating earthquakes (Taymaz et al., 1991; Ambraseys and Jackson, 1998; Tan O and Taymaz, 2006). Notably, a pronounced seismic gap persists along the southern EAFZ segment, where the last documented rupture before the 2023 M_w 7.8 event was the M_s 7.4 Earthquake in 1513. Long-term strain accumulation within this gap may be the principal driver of the 2023 Kahramanmaraş Earthquake.

Since the 2023 Türkiye Earthquake doublet, numerous studies have been published (Gabriel et al., 2023; Jia Z et al., 2023; Liu CL et al., 2023; Melgar et al., 2023; Rosakis et al., 2023; Ren CM et al., 2024; Li B et al., 2025). Most results indicate a complex rupture process for the M_w 7.8 event, with ongoing debates over the nucleation site on the main fault and rupture velocity on the branch fault. Using InSAR (interferometric synthetic aperture radar) data, seismic records, and aftershock locations to constrain the fault model and joint inversion to resolve the rupture process, Liu CL et al. (2023) proposed that rupture on the main fault nucleated at the triple junction between the main fault and the branch fault and propagated bilaterally; Melgar et al. (2023) also supports this interpretation. Integrating multi-scale seismic and geodetic records with kinematic inversion and dynamic rupture simulations, Jia Z et al. (2023) inferred that rupture on the main fault first propagated toward the northeast, and after a delay extended southwestward. Similar findings were reported by Wang ZJ et al. (2023) and Li B et al. (2025). In contrast, Ren CM et al. (2024), through joint inversion of near- and far-field seismic waveforms, GNSS (Global Navigation Satellite System) data, and the waveform polarization direction, concluded that the main fault nucleated ~9 km west of the triple junction and subsequently ruptured bilaterally. Considering the complex rupture process of the M_w 7.8 Kahramanmaraş event, resolving the nucleation site on the main fault is critical for understanding the triggering mechanism involving the Narlı branch fault.

The interpretation of rupture velocity along the Narlı branch fault also remains inconsistent. Rosakis et al. (2023) analyzed the ratio and waveforms of fault-parallel and fault-normal components from two near-fault stations (4615 and NAR, as shown in Figure 1) and inferred that supershear rupture occurred ~19 km from the epicenter on the Narlı branch fault. In contrast, Melgar et al. (2023), through kinematic multiple-time-window inversion, characterized the overall Narlı branch fault as subshear. Li B et al. (2025) also indicated through dynamic simulations that supershear velocity is not necessary to extend a rupture to the main fault. For the main fault, Jia Z et al. (2023) indicated a rupture velocity of 3.2 km/s along the northeastern segment, consistent with subshear rupture, whereas Ren CM et al. (2024) and Li B et al. (2025) concluded that the northeastern segment exhibited supershear characteristics.

In this study, we integrate relocated aftershock data, surface rupture traces, GNSS observations, and near-field strong ground motion records to construct a three-dimensional (3D) dynamic rupture model of the 2023 M_w 7.8 Kahramanmaraş Earthquake. Finite fault solutions are used to constrain the stress drop on the fault plane. Through 3D dynamic rupture simulations, we compare synthetic results with recorded seismic station data and GPS data to constrain the nucleation location where rupture propagated from the branch fault to the EAF during the 2023 M_w 7.8 Kahramanmaraş Earthquake.

2. Model and Method

Dynamic rupture simulations provide valuable insight into the triggering mechanism of Narlı branch faults on the main fault. However, key simulation parameters, such as fault geometry, background stress distribution, and friction parameters, are still difficult to constrain directly through *in situ* measurements.

From the surface fault trace data provided by Reitman et al. (2023) and the aftershock relocation results from Melgar et al. (2023), we construct a 3D nonplanar fault model for the 2023 M_w 7.8 Kahramanmaraş Earthquake event. We retain only the Narlı fault where the mainshock occurred and exclude minor branch faults (Melgar et al., 2023). The M_w 7.8 Kahramanmaraş Earthquake ruptured more than 350 km along three primary faults—the Amanos, Pazarcık, and Erkenek Faults—and the Narlı branch faults. Our fault dataset comprises approximately 150 scattered points distributed along a roughly 380-km-long fault system. These points are projected onto specific depth levels (0, 10, 15, and 20 km) according to their depth ranges, and smooth curves are fitted at each depth to generate four constraining lines. We then apply the spline-constraint method in Gmsh to construct the fault model. The overall fault dip angle is 85°, decreasing to 80° in the northeastern Erkenek segment, consistent with the results of Melgar et al. (2023). The fault width is 20 km.

In our study, we adopt the slip-weakening law as follows (Andrews, 1976):

$$\tau = \begin{cases} \tau_d + (\tau_p - \tau_d) \times (1 - \delta/D_c), & 0 \le \delta < D_c, \\ \tau_d, & \delta \ge D_c. \end{cases} \tag{1}$$

Here, τ represents the frictional stress at a cumulative slip δ; $\tau_p = \mu_s \sigma_n$ denotes the yield strength, where μ_s is the static friction coefficient and σ_n is the normal stress; $\tau_d = \mu_d \sigma_n$ is the residual stress, where μ_d the dynamic friction coefficient; and D_c is the critical slip-weakening distance. Khalifa et al. (2018) examined rock strength near the EAF and noticed substantial spatial variations along its segments. Accordingly, we assign different static and dynamic friction coefficients along the EAF. We set $\mu_s = 0.4$ and $\mu_d = 0.21$ for the Narlı fault segment, and $\mu_s = 0.412$ and $\mu_d = 0.12$ for the EAF segment. The characteristic slip distance D_c is 0.2 m within the depth range of 0–20 km.

Initial stresses, a critical parameter controlling rupture dynamics, remain challenging to constrain for historical earthquakes. Li B et al. (2025) integrated seismotectonic observations, assumptions of fault-zone fluid overpressure, and the Mohr–Coulomb failure criterion to constrain segment-specific orientations of maximum principal stress in the EAF region. Following Li B et al. (2025), we assign maximum principal stress directions ranging from N170°E and N205°E, divided into four segments according to the fault location (as shown in Figure 2b). Notably, the maximum principal stress orientations on branch faults deviate substantially from those in adjacent EAF segments, which we attribute to localized tectonic rotation.

We define the initial triaxial principal stresses. They vary with depth within the upper 3 km but remain constant below a depth of 3 km to prevent an excessive stress drop at the fault base. The vertical principal stress is given by

$$\sigma_{zz} = \rho g z (1 - \gamma), \tag{2}$$

where ρ denotes the rock density and γ is the pore pressure factor, adopted as 0.71 in this study. The stress regime ratio R, defined as $R = (S_v - S_H)/(S_h - S_H)$, is also important to constrain the initial stress, where S_h, S_H, S_v are the minimum, maximum, and vertical principal stress, respectively. Using the focal mechanism inversion results, Yilmaz et al. (2006) proposed an average R value of 0.715 in the north part of the EAF. In our model, R is set to 0.7 for the northeastern segment of the EAF and the Narlı fault, consistent with the dominant transpressional tectonic regime in this region. In contrast, for the southwestern segment of the EAF, which is characterized by a transtensional tectonic environment (Lyberis et al., 1992), R is assigned as 0.3. Another controlling factor, $k = S_H/S_v$, is set to 1.5 for the northeastern segment of the EAF and the Narlı fault and to 1.1 for the southwestern segment of the EAF.

We project the triaxial principal stresses onto the fault plane to obtain the initial normal stress σ_n distribution (Figure 2a). Heterogeneous initial shear stresses τ_0 based on the kinematic slip model are further introduced. Ren CM et al. (2024) provided a reference distribution of fault slip. We calculate the stress drops on the fault by using the slip model and the Okada model (Okada, 1985, 1992). The residual stress τ_d is derived from the normal stress and the dynamic friction coefficient. Superimposing the residual stress

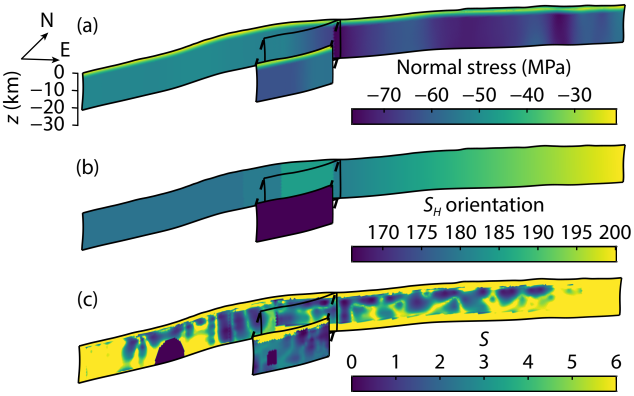

Figure 2. (a) Normal stress distribution on the fault, obtained by projecting the triaxial stress onto the fault plane; (b) maximum principal stress orientation of the S_H; (c) S-value distribution along the fault plane.

and the calculated stress drop yields the initial stress distribution on the fault (Figure 3a). The stress intensity parameter S (defined as $(\tau_p - \tau_0)/(\tau_0 - \tau_d)$) is distributed as shown in Figure 2c. The distribution of the S-value indicates that large asperities predominantly occur along geometrically continuous and planar fault segments (Zhang YJ et al., 2023). By comparing simulated ground motion with recorded station data and GPS records through trial and error, we develop three distinct stress models. The stresses illustrated in Figure 3a are designated as Model 1. On the basis of Model 1, we introduce an additional stress perturbation in the localized regions to the southwest of the triple junction of the EAF to define Model 2 (Figure 3b). As shown in Figure 3c, Model 3 shares the same initial stresses as Model 2 except for the Narlı branch fault, where the initial shear stress is higher. The hypocenter location is assigned based on high-precision hypocenter relocation results from Melgar et al. (2023) and is situated ~35 km from the triple junction along a branch fault at a depth of 12 km. The radius of the nucleation zone is 3.5 km. The initial shear stress of the nucleation zone is set 0.1 MPa higher than the yield strength to trigger rupture. Our model incorporates the 3D velocity structure in the EAFZ derived by Wang Z et al. (2024) using double-difference tomography integrated with multi-parameter seismic tomography. The density is calculated following the empirical equation (Brocher, 2005).

We utilize the open-source software drdg3d, developed by Zhang WQ et al. (2023), to simulate the dynamic rupture processes of the 2023 M_w 7.8 Kahramanmaraş Earthquake. The drdg3d software utilizes a discontinuous Galerkin (DG) method with tetrahedral meshes (Hesthaven and Warburton, 2008) and has been widely adopted for dynamic rupture simulations of earthquakes (Ramos et al., 2021; Biemiller et al., 2022; Wang ZJ et al., 2023). The drdg3d method incorporates a hybrid numerical flux combining upwind and central fluxes, thereby reducing mesh dependency and enhancing computational efficiency. The method has demonstrated excellent performance across multiple benchmark models in the Statewide California Earthquake Center (SCEC)/ U.S. Geological Survey (USGS) Spontaneous Rupture Code Verification Project (https://strike.scec.org/cvws/; Harris et al., 2009). To raise computational efficiency, our model utilizes a grid size of 1 km with third-order spatial accuracy. The time step is 0.07 s, and the total simulation time is 85 s.

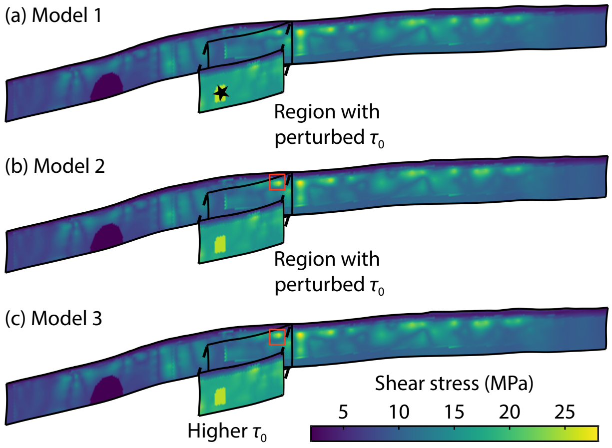

Figure 3. Initial heterogeneous shear stress τ_0 distribution on the fault of Models 1–3. The initial shear stress is obtained by superimposing the residual stress (derived from the normal stress in Figure 2a) onto the stress drop inferred from the coseismic slip distribution of Ren CM et al. (2024). (a) Shear stress of Model 1, where the black star marks the hypocenter; (b) shear stress of Model 2, the same as Model 1 except that the initial shear stress is higher in the region with perturbed τ_0; (c) shear stress of Model 3, the same as Model 2 except with higher initial shear stress on the Narlı branch fault.

3. Results and Discussion

3.1 Results of Model 1

The slip rate snapshots of Model 1 are shown in Figure 4. Following nucleation on the Narlı branch fault, a clear supershear rupture daughter crack emerges at 8.3 s, consistent with previous studies (Abdelmeguid et al., 2023; Rosakis et al., 2023; Wang ZJ et al., 2023; Ren CM et al., 2024). The rupture reaches the end of the branch fault by ~13.4 s. At 16 s, the rupture transfers to the main fault at the triple junction and begins propagating northeastward. By 20 s, the rupture also initiates southwestward along the main fault. Subsequently, because of the complex fault geometry, the rupture velocity exhibits significant variation across different segments. Notably, supershear rupture occurs on both the northeastern and southwestern segments by ~59 s. Our results are consistent with the findings of Abdelmeguid et al. (2023) and Yao SL and Yang HF (2025). Moreover, the rupture transits from crack-like to pulse-like rupture at 59 s because the fault length is much longer than the fault width. The stopping phase from the top and bottom of the fault provides the healing effect.

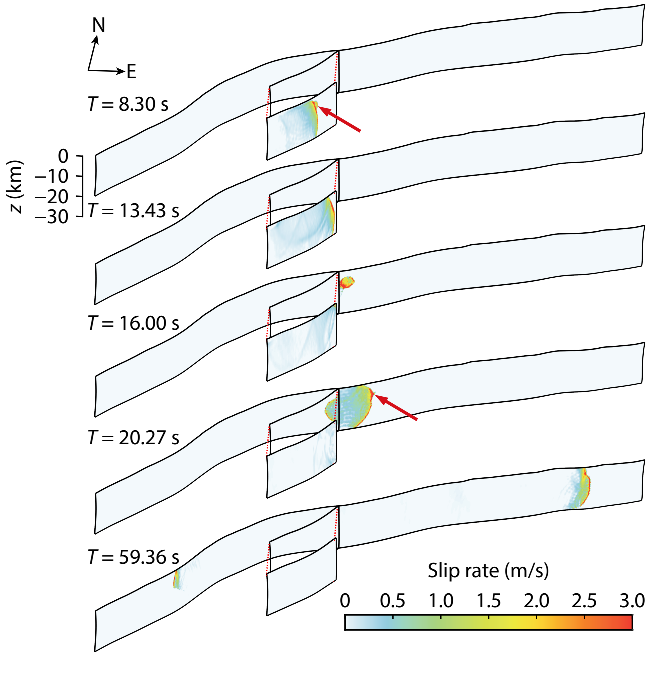

Figure 4. Slip rate snapshots of Model 1. The red arrows indicate the supershear rupture.

The final slip (Figure 5b) shows good agreement with the kinematic inversion result by Ren CM et al. (2024). A large asperity with the peak slip of ~8.1 m is located northeast of the triple junction on the Pazarcık Fault, consistent with the results of previous studies (Melgar et al., 2023; Chen KJ et al., 2024; Ren CM et al., 2024; Li B et al., 2025). Slip on the Amanos Fault is smaller than that on the Pazarcık Fault and the Erkenek Fault. A prominent bend appears to act as a barrier to rupture propagation. The theoretical moment magnitude is M_w 7.85, which aligns closely with the observation. We also simulate ground motion at the stations marked by black triangles in Figure 1. Figure 5a compares the simulated and observed seismographs, both low-pass filtered at 0.4 Hz. Our results successfully reproduce the primary characteristics of the recorded waveforms. Stations near the triple junction (e.g., NAR, 4614, and 4624) clearly show two distinct wave peaks corresponding to ruptures on the Narlı branch fault and the main fault, respectively, where stations farther away exhibit a single dominant pulse. The arrival times of the main peaks at different stations show good agreement with observations. Additionally, we calculate the surface horizontal displacement field by using an elastic half-space dislocation model (Meade, 2007; Nikkhoo and Walter, 2015) and compare the results with GPS observations (Figure 5c). The simulated displacement pattern generally agrees with the measured data, although some discrepancies in vector direction and magnitude remain, probably owing to greater spatial heterogeneity in the actual slip distribution.

Thus, Model 1 generates a rupture process that nucleates on the Narlı branch fault, propagates to the triple junction of the main fault, initially extends unilaterally northeastward along the main EAF, and, after a delay of several seconds, subsequently propagates southward. This rupture sequence aligns well with the results of

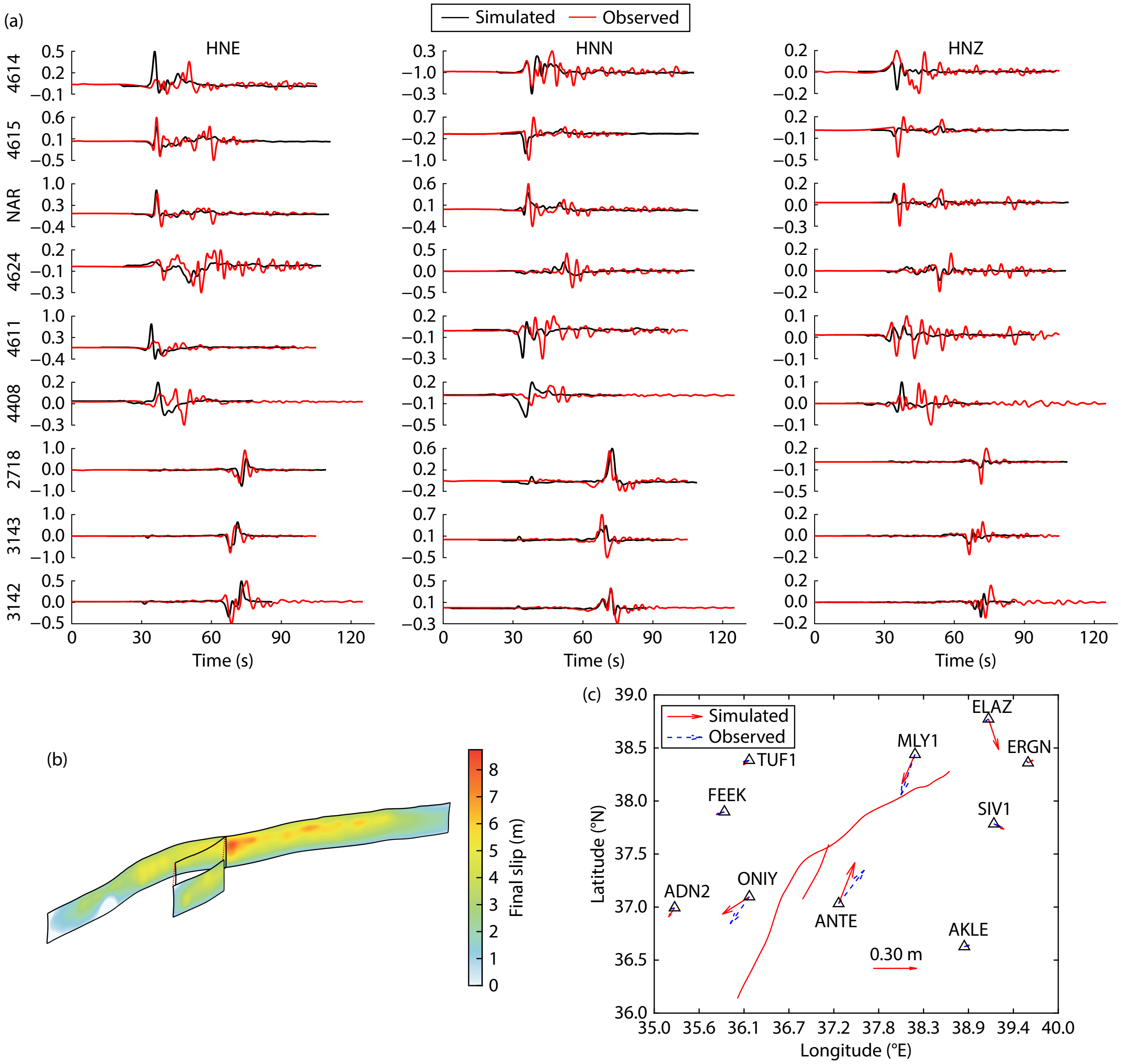

Figure 5. (a) Comparison of simulated waveforms of Model 1 and recorded velocity waveforms from different stations; (b) final slip distribution of Model 1; (c) comparison between simulated and observed surface GPS displacements.

Jia Z et al. (2023) and Li B et al. (2025). However, unlike those of Ren CM et al. (2024), we do not observe nucleation ~9 km southwest of the triple junction on the main fault.

3.2 Effect of Perturbed Stress along the EAF

Kame et al. (2003) performed a series of two-dimensional (2D) simulations on branched fault systems and demonstrated that rupture velocity, initial stress distribution, and fault branching angle jointly determine the rupture path. In Model 1, the heterogeneous initial stress combined with the complex fault geometry produces the complicated rupture process of the 2023 M_w 7.8 Kahramanmaraş event. However, as illustrated in Figure 4, this stress concentration is insufficient to trigger nucleation when rupture propagates from the Narlı branch to the EAF main strand. To investigate the stress perturbation effect of controlling the nucleation location of the Narlı branch fault to the main EAF strand, we modify Model 2 by perturbing the initial stress within a localized 3 km × 3 km patch (red rectangle in Figure 3b) by an additional 2.5 MPa. This patch is centered ~9 km to the southwest of the triple junction (Figure 3b) and coincides spatially with the potential nucleation site on the main EAF proposed by Ren CM et al. (2024). The corresponding slip rate snapshots are shown in Figure 6.

The rupture process along the Narlı branch of Model 2 is identical to that in Model 1. However, after the rupture jumps onto the main strand of the EAF, nucleation initiates at ~13 s at a location ~9 km to the southwest of the triple junction. The rupture then propagates southwestward. By 16 s, a second nucleation patch occurs in the northeast EAF, resulting in two distinct bilateral rupture fronts. These two rupture fronts eventually coalesce into a single large event around 20 s. The primary difference from Model 1 is the earlier onset of nucleation and subsequent bilateral propagation ~9 km to the left of the triple junction. This rupture pattern coincides with the finding of Ren CM et al. (2024).

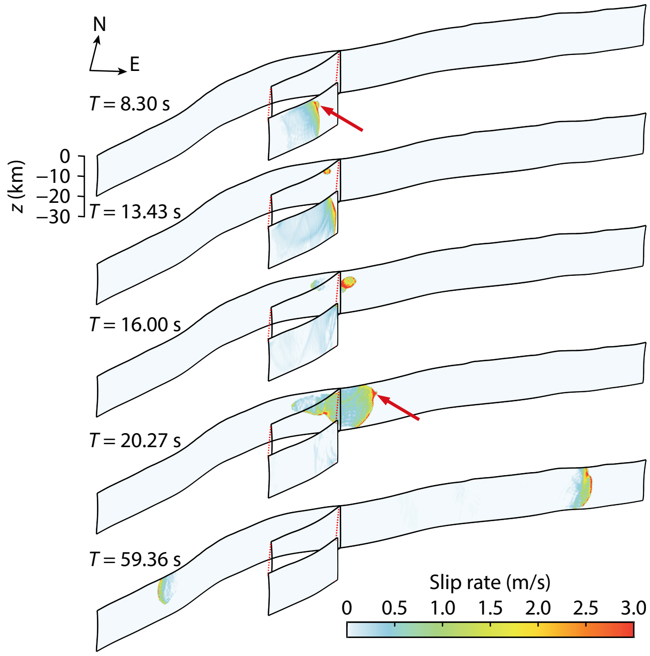

Figure 6. Slip rate snapshots of Model 2. The red arrows indicate the daughter crack that marks the supershear rupture.

However, Ren CM et al. (2024) suggested that the rupture at the triple junction arises from the combined effects of the southwest-nucleated rupture and the incoming rupture from the Narlı branch—leading to an immediate supershear transition after passing the triple junction. Our Model 2 results indicate that the rupture at the triple junction is primarily driven by the wave from the Narlı branch fault, with the southwest-nucleated rupture arriving only after slip has already initiated at the junction.

The final slip distribution of Model 2 is shown in Figure 7b with a peak slip of ~8.1 m located to the northeast of the triple junction, similar to Model 1. The calculated moment magnitude is M_w 7.86, slightly higher than the M_w 7.85 of Model 1. The locations and extents of major asperities in Model 2 closely resemble those in Model 1. This similarity indicates that differences in nucleation locations near the triple junction do not significantly influence the primary characteristics of the heterogeneous slip distribution observed in the 2023 M_w 7.8 event. Consistent with the similar slip distributions (Figure 7a), the simulated strong ground motion velocity waveforms at near-fault stations in Model 2 match the recorded waveforms well. Similarly, the modeled horizontal surface displacements agree closely with GPS observations (Figure 7c). The most notable difference between the two models occurs within the region highlighted by the red box in Figure 3b, where Model 2 exhibits greater slip owing to a significantly larger stress drop. However, because the overall prestress field remains nearly identical between the two models, the large-scale patterns of the final slip distribution show no substantial differences.

Comparison of the results from Model 1 and Model 2 reveals that premature nucleation to the southwest of the triple junction on the EAF requires a significantly elevated local stress level in that region. This result indicates that the nucleation barrier to the southwest of the triple junction is substantially greater than at the triple junction itself.

A similar observation was reported by Ding XT et al. (2023), who simplified the fault system of the 2023 Kahramanmaraş Earthquake sequence into a 2D planar branched fault system and examined the temporal evolution of dynamic Coulomb failure stress, ΔCFS, at different locations along the main fault under varying model conditions. Here, ΔCFS quantifies the change in Coulomb failure stress during rupture propagation ($\Delta\mathrm{CFS} = \Delta\tau + \mu \times \Delta\sigma_n$), where positive values promote failure and negative values inhibit it. In the study by Ding XT et al. (2023), a zone of positive ΔCFS appears to the southwest of the triple junction before the rupture front arriving from the branch fault reaches the junction, indicating that premature nucleation in that region is theoretically possible. However, the magnitude of ΔCFS at the triple junction itself is markedly larger than in the adjacent southwest region. Consequently, nucleation to the southwest of the triple junction demands a locally elevated initial shear stress.

3.3 Effect of Rupture Velocity along the Narlı Branch

To examine how rupture velocity on the Narlı branch fault influ-

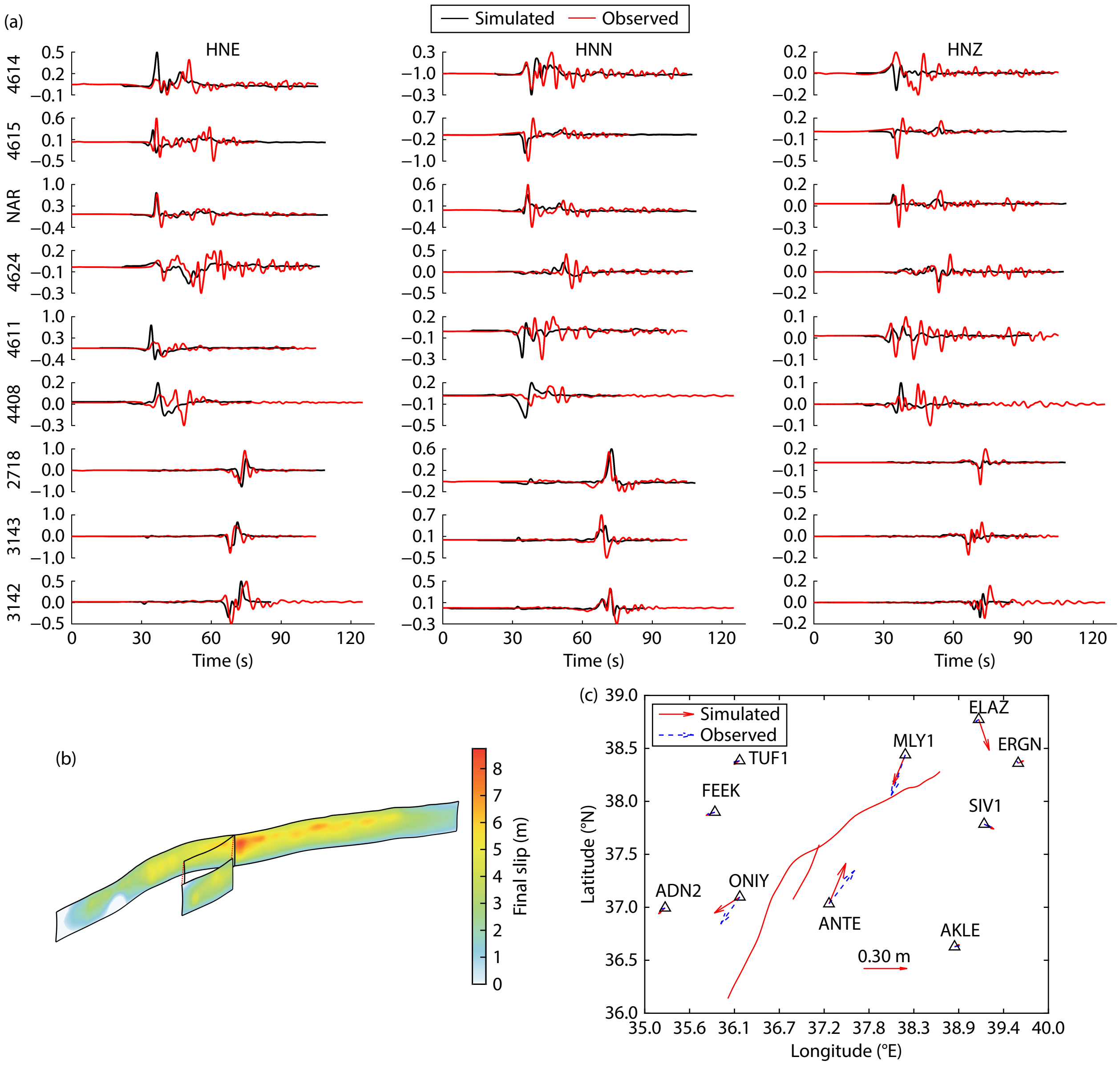

Figure 7. (a) Comparison of simulated velocity waveforms of Model 2 and recorded velocity waveforms at different stations; (b) final slip distribution on the fault plane of Model 2; (c) comparison between simulated and observed surface GPS displacements.

ences nucleation on the main fault, we construct Model 3 by systematically increasing the initial shear stress on the branch fault relative to Model 2 except for the prescribed nucleation patch. As shown in Figures 3b and 3c, the initial shear stress on the branch fault in Model 3 is uniformly raised by ~2 MPa everywhere except within the prescribed nucleation patch. Figure 8 displays the rupture arrival time versus along-strike distance on the Narlı branch fault. After nucleation, the rupture speeds on the branch fault of both Model 2 and Model 3 are 3.6 km/s, slightly larger than the S-wave speed (3.4 km/s). In Model 2, the rupture speed shortly accelerates to 4.0 km/s because of the high-stress zone there, and then decreases to 3.2 km/s, the sub-Rayleigh speed, to the end of the branch fault. In Model 3, however, the stress perturbation initiates a daughter crack in the high-stress zone, which further accelerates to 5.4 km/s, close to the P-wave speed, to the end of the Narlı branch fault.

The slip rate snapshot of Model 3 is shown in Figure 9. Supershear rupture on the branch fault becomes prominent at ~8.3 s on the upper side of the fault, earlier than the 10 s in Model 2, where the transition to supershear occurs near the end of the branch fault. When the rupture transfers to the main EAF at ~13 s, no premature nucleation is observed at the location 9 km southwest of the triple junction, although the high initial stress perturbation still exists there. In Model 3, nucleation initiates directly at the triple junction on the main EAF and propagates northeastward. By 16 s, the high-stress zone southwest to the triple junction also nucleates, leading to bilateral rupture propagation along the main EAF. Supershear rupture still occurs to the northeast of the triple junction.

We attribute the contrasting nucleation behavior between Model 2 and Model 3 to differences in dynamic energy radiation from the Narlı branch fault. Ren CM et al. (2024) proposed that supershear

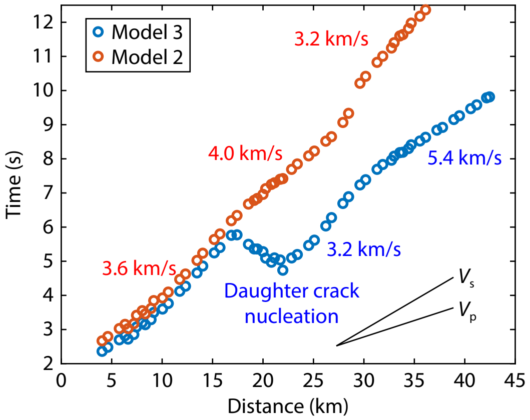

Figure 8. Comparison of rupture velocity along the strike at 5 km depth between Model 2 and Model 3. The distance of 0 km refers to the nucleation point on the branch fault.

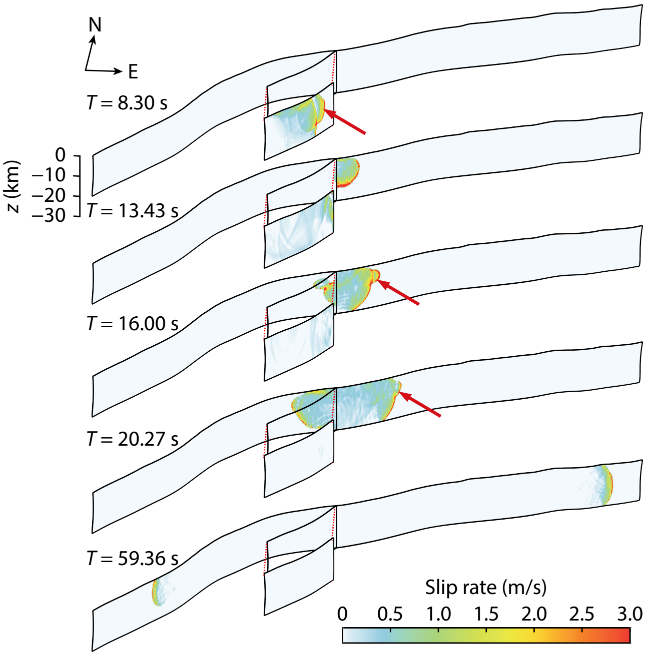

Figure 9. Slip rate snapshots of Model 3. The red arrows indicate the supershear rupture.

rupture on the branch fault of the 2023 M_w 7.8 Kahramanmaraş event triggered premature nucleation ~9 km southwest to the triple junction on the main EAF. Both Model 2 and Model 3 exhibit clear supershear rupture behavior along the branch fault, but the rupture velocity of Model 3 is higher. Compared with subshear rupture, supershear rupture confines energy radiation within the Mach cone. The Mach angle is defined as $\theta = \arcsin(V_s/V_r)$, where V_r is the rupture velocity and V_s is the shear wave velocity. A higher rupture velocity yields a smaller Mach angle, resulting in a narrower Mach cone and more focused energy radiation. Therefore, because the rupture velocity on the branch fault is higher in Model 3, the Mach cone covers a smaller area, leading to a reduced positive ΔCFS perturbation to the southwest of the triple junction on the main fault. This prevents nucleation at 9 km southwest of the triple junction, as shown in the slip rate snapshots in Model 3.

Figure 10 compares the source time functions of Models 1–3 and the USGS result. All three models reproduce the observed total rupture duration of ~70–80 s and the concentration of moment release between 20 s and 50 s, characterized by two prominent peaks. The first peak (20–30 s) reflects nucleation on the main EAF near the triple junction and bilateral propagation, dominated by the first large slip asperity northeast of the triple junction. The second peak (40–50 s) corresponds to rupture extension onto the southwestern Amanos segment and the northeastern Erkenek segment, with an additional contribution from the second major asperity northeast of the triple junction. The second peak arrival time of Model 2 coincides well with the USGS result, whereas those of Model 1 and Model 3 are slightly earlier. Notably, Model 3 shows a pronounced early peak at 5–15 s that is absent in the USGS result, indicating that this P-wave approaching rupture velocity on the branch fault is unrealistic for the 2023 M_w 7.8 event.

4. Conclusion

We construct a 3D fault geometry for the 2023 M_w 7.8 Kahramanmaraş Earthquake based on surface fault trace data (Reitman et al., 2023) and relocated aftershocks (Melgar et al., 2023). We then develop heterogeneous initial stresses along the fault, constrained by the kinematic slip inversion (Ren CM et al., 2024), near-field seismogram, and GPS observations. We present three different dynamic rupture models to investigate the nucleation behavior near the triple junction of the main EAF.

Model 1 reproduces the inverted slip distribution, observed near-field seismic waveforms, and GPS observations. Following nucleation on the Narlı branch fault, where supershear rupture occurs, rupture nucleates near the triple junction and propagates northeastward first. Nearly 4 s later, the rupture also propagates southwest toward the Amanos Fault. To facilitate nucleation at 9 km southwest of the triple junction of the main EAF, as hypothesized by Ren CM et al. (2024), an artificially elevated initial shear stress is required in that region, as shown in Model 2. However, this nucleation difference itself does not greatly influence the overall characteristics of the final slip distribution, near-field ground motion, and surface displacement, demonstrating that the complex 3D geometry and rupture process mask early nucleation details. Thus,

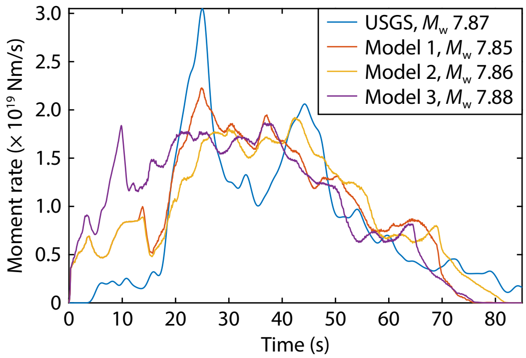

Figure 10. The comparison of source time functions among Models 1–3 and the USGS result.

both nucleation locations, the triple junction and 9 km southwest of the triple junction, are possible for the 2023 M_w 7.8 Kahramanmaraş event. However, the triple junction is more likely to nucleate because of the positive dynamic Coulomb stress perturbation there, whereas the condition for the southwest nucleation is stricter—a higher initial shear stress perturbation is necessary. Moreover, we elevate the initial shear stress along the Narlı branch fault in Model 3, which increases the rupture velocity before the rupture transfers to the main EAF, and the P-wave approaching supershear rupture velocity results in a narrower Mach cone, making the southwest nucleation on the main EAF more difficult, although the comparison of source time function of the three models and the USGS result indicates such a P-wave approaching supershear speed is less likely for the 2023 M_w 7.8 event. Our models reconcile kinematic interpretation of the 2023 M_w 7.8 Kahramanmaraş Earthquake and highlight the critical role of branch-fault rupture velocity and initial stress perturbation in controlling rupture transfer across complex fault junctions.

Acknowledgments

We thank Editor HuaJian Yao and the two anonymous reviewers for their constructive reviews and insightful comments, which helped improve the manuscript. This study was supported by the National Natural Science Foundation of China (Grant No. 42074049) and the Youth Innovation Promotion Association of the Chinese Academy of Sciences (Grant No. 2023471). The numerical calculations were done at the Hefei Advanced Computing Center. We also thank Jian Wen for managing the local cluster for us to test the model.

Data Availability

The dynamic rupture software drdg3d is available at https://github.com/wqseis/drdg3d or https://doi.org/10.5281/zenodo.8000437 (Zhang WQ et al., 2023, last accessed April 2026). We obtained the curve fault model data from https://zenodo.org/record/7699971#.ZATVUhPMLnw (Melgar et al., 2023). We obtained the strong ground motion data from the Turkish National Strong Motion Network through the Disaster and Emergency Management Presidency of Türkiye (AFAD, https://tadas.afad.gov.tr). The slip distribution data can be found at https://www.science. org/doi/10.1126/science.adi1519 (Ren CM et al., 2024). The GPS data used can be found at https://zenodo.org/record/7699971#.ZATVUhPMLnw (Melgar et al., 2023). The source time function data of USGS can be found at https://earthquake.usgs.gov/earthquakes/eventpage/us6000jllz/executive.

Supplementary Materials

A Stress Parameter Uncertainty Analysis

In the following section, we slightly change two different parameters of the stress (D_c and μ_d) to test the parameter uncertainties.

S1. D_c Uncertainty

In our previous model, we set 0.2 m as the value of D_c. However, in this section, we change D_c to 0.4 m to observe the results. Other stress parameters stay the same as in Model 2.

In Figure S1, the waveform comparison result also aligns well with the result of Model 2. However, the peak slip is only 7 m, smaller than the result of Model 2. So, under the stress conditions we set, we consider D_c = 0.2 m as a more appropriate value. Notably, if we set D_c to 0.8 m, the rupture cannot even break through the nucleation zone.

S2. μ_d Uncertainty

The setting of friction parameters refers to Wang ZJ et al. (2023), but their friction parameters are more heterogeneous. We simplify the condition. In our model, we set μ_d = 0.2 for the Narlı branch fault. For the main EAF, the μ_d is 0.12. However, within the same fault system, this difference is strikingly abnormal. So we set μ_d = 0.2 in the main fault, keeping it the same as with the branch fault. Other stress parameters are the same as with Model 2.

In our model, we superimpose the residual stress and the stress drop to obtain the initial shear stress. As we raise the value of μ_d, the stress drop is higher, so the initial shear stress of the main fault is larger than in Model 2.

In Figure S2a, the simulated waveform does not fit well with the observed data. In addition, the peak slip in Figure S2b is 9 m, obviously larger than in Model 2, whose peak slip is 8.1 m. Therefore, under the stress conditions of our model, we think this result is implausible.

References

Abdelmeguid, M., Zhao, C. H., Yalcinkaya, E., Gazetas, G., Elbanna, A., and Rosakis, A. (2023). Dynamics of episodic supershear in the 2023 M7.8 Kahramanmaraş/Pazarcik Earthquake, revealed by near-field records and computational modeling. *Commun. Earth Environ.*, *4*, 456. https://doi.org/10.1038/s43247-023-01131-7

Ambraseys, N. N. (1989). Temporary seismic quiescence: SE Turkey. *Geophys. J. Int.*, *96*(2), 311–331. https://doi.org/10.1111/j.1365-246X.1989.tb04453.x

Ambraseys, N. N., and Jackson, J. A. (1998). Faulting associated with historical and recent earthquakes in the Eastern Mediterranean region. *Geophys. J. Int.*, *133*(2), 390–406. https://doi.org/10.1046/j.1365-246X.1998.00508.x

Andrews, D. J. (1976). Rupture velocity of plane strain shear cracks. *J. Geophys. Res.*, *81*(32), 5679–5687. https://doi.org/10.1029/JB081i032p05679

Barbot, S., Luo, H., Wang, T., Hamiel, Y., Piatibratova, O., Javed, M. T., Braitenberg, C., and Gurbuz, G. (2023). Slip distribution of the February 6, 2023 Mw 7.8 and Mw 7.6, Kahramanmaraş, Turkey earthquake sequence in the East Anatolian Fault Zone. *Seismica, 2*(3). https://doi.org/10.26443/seismica.v2i3.502

Biemiller, J., Gabriel, A. A., and Ulrich, T. (2022). The dynamics of unlikely slip: 3D modeling of low-angle normal fault rupture at the Mai'iu fault, Papua New Guinea. *Geochem. Geophys. Geosyst.*, *23*(5), e2021GC010298. https://doi.org/10.1029/2021gc010298

Brocher, T. M. (2005). Empirical relations between elastic wavespeeds and density in the Earth's crust. *Bull. Seismol. Soc. Am.*, *95*(6), 2081–2092. https://doi.org/10.1785/0120050077

Chen, K. J., Wei, G. G., Milliner, C., Zilio, L. D., Liang, C. R., and Avouac, J. P. (2024). Super-shear ruptures steered by pre-stress heterogeneities during the 2023 Kahramanmaras earthquake doublet. *Nat. Commun.*, *15*, 7004. https://doi.org/10.1038/s41467-024-51446-y

Delouis, B., van den Ende, M. P. A., and Ampuero, J. P. (2023). Kinematic rupture model of the February 6th 2023 Mw 7.8 Turkey earthquake from a large set of near-source strong motion records combined by GNSS offsets reveals intermittent supershear rupture. *Earth Planet. Phys.*, *7*(6), 691–709. https://

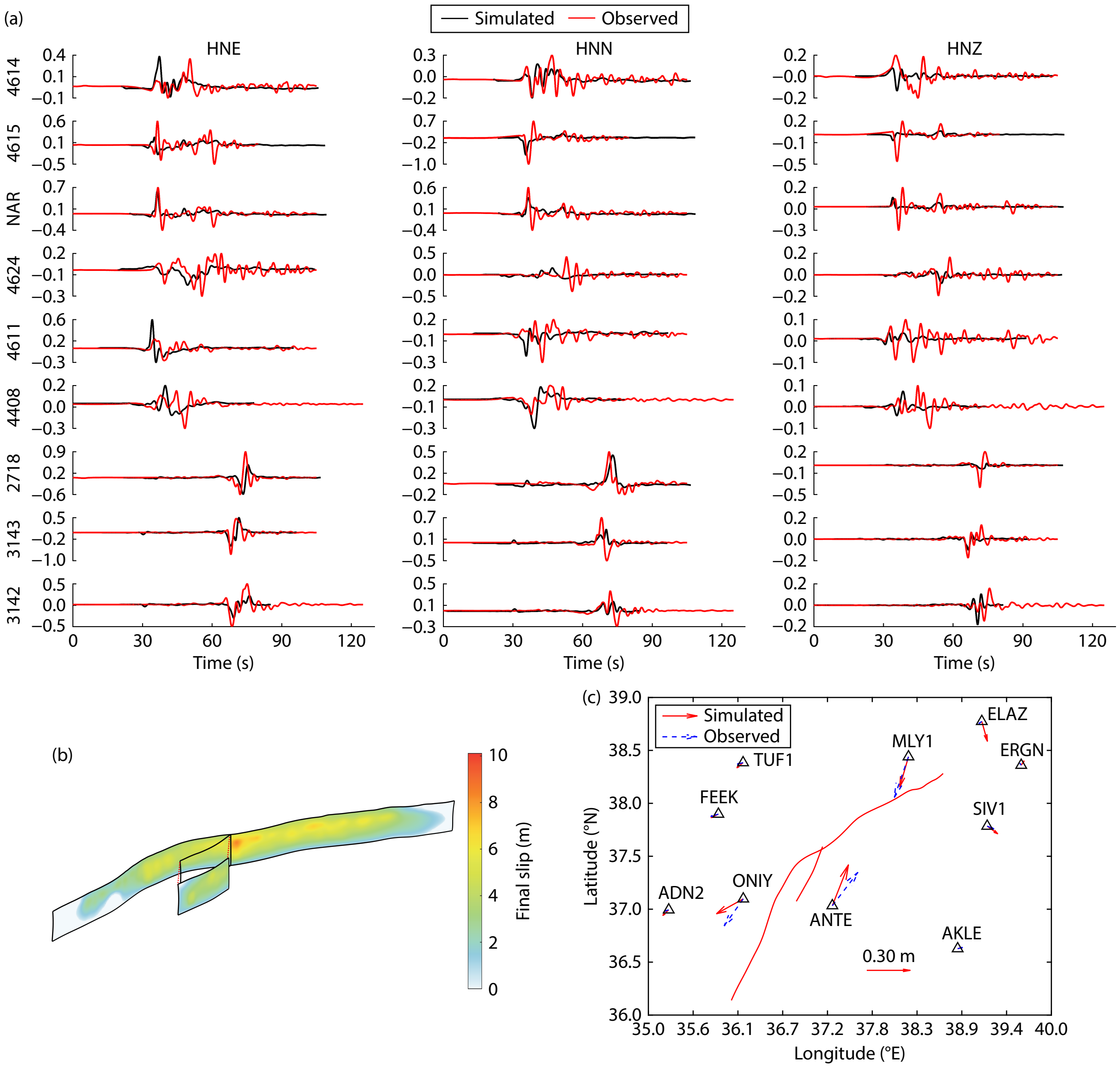

Figure S1. (a) Comparison of simulated velocity waveforms and recorded velocity waveforms at different stations; (b) final slip distribution on the fault plane; (c) comparison between simulated and observed surface GPS displacements.

doi.org/10.22541/essoar.168286647.71550161/v1

Ding, X. T., Xu, S. Q., Xie, Y. Q., van den Ende, M., Premus, J., and Ampuero, J. P. (2023). The sharp turn: Backward rupture branching during the 2023 Mw 7.8 Kahramanmaraş (Türkiye) earthquake. *Seismica*, *2*(3), 1–17. https://doi.org/10.26443/seismica.v2i3.1083

Gabriel, A. A., Ulrich, T., Marchandon, M., and Biemiller, J. (2023). Geodetically and seismically informed rapid 3D dynamic rupture modeling of the Mw7.8 Kahramanmaraş earthquake. In *EGU General Assembly 2023* (pp. EGU23–17603). Vienna, Austria: EGU. https://doi.org/10.5194/egusphere-egu23-17603

Harris, R. A., Barall, M., Archuleta, R., Dunham, E., Aagaard, B., Ampuero, J. P., Bhat, H., Cruz-Atienza, V., Dalguer, L., … Templeton, E. (2009). The SCEC/USGS dynamic earthquake rupture code verification exercise. *Seismol. Res. Lett.*, *80*(1), 119–126. https://doi.org/10.1785/gssrl.80.1.119

Hesthaven, J. S., and Warburton, T. (2008). *Nodal Discontinuous Galerkin Methods: Algorithms, Analysis, and Applications*. New York: Springer. https://doi.org/10.1007/978-0-387-72067-8

Ida, Y. (1972). Cohesive force across the tip of a longitudinal-shear crack and Griffith's specific surface energy. *J. Geophys. Res.*, *77*(20), 3796–3805. https://doi.org/10.1029/JB077i020p03796

Jia, Z., Jin, Z. Y., Marchandon, M., Ulrich, T., Gabriel, A. A., Fan, W. Y., Shearer, P., Zou, X. Y., Rekoske, J., … Fialko, Y. (2023). The complex dynamics of the 2023 Kahramanmaraş, Turkey, M_w 7.8–7.7 earthquake doublet. *Science*, *381*(6661), 985–990. https://doi.org/10.1126/science.adi0685

Kame, N., Rice, J. R., and Dmowska, R. (2003). Effects of prestress state and rupture velocity on dynamic fault branching. *J. Geophys. Res.: Solid Earth*, *108*(B5), 2265. https://doi.org/10.1029/2002JB002189

Khalifa, A., Çakır, Z., Owen, L. A., and Kaya, Ş. (2018). Morphotectonic analysis of the East Anatolian fault, Turkey. *Turkish J. Earth Sci.*, *27*(2), 110–126. https://doi.org/10.3906/yer-1707-16

Li, B., Palgunadi, K. H., Wu, B. N., Suhendi, C., Zhou, Y. J., Ghosh, A., and Mai, P. M. (2025). Rupture dynamics and velocity structure effects on ground motion during the 2023 Türkiye earthquake doublet. *Commun. Earth Environ.*, *6*(1), 228. https://doi.org/10.1038/s43247-025-02205-4

Liu, C. L., Lay, T., Wang, R. J., Taymaz, T., Xie, Z. J., Xiong, X., Irmak, T. S., Kahraman, M., and Erman, C. (2023). Complex multi-fault rupture and

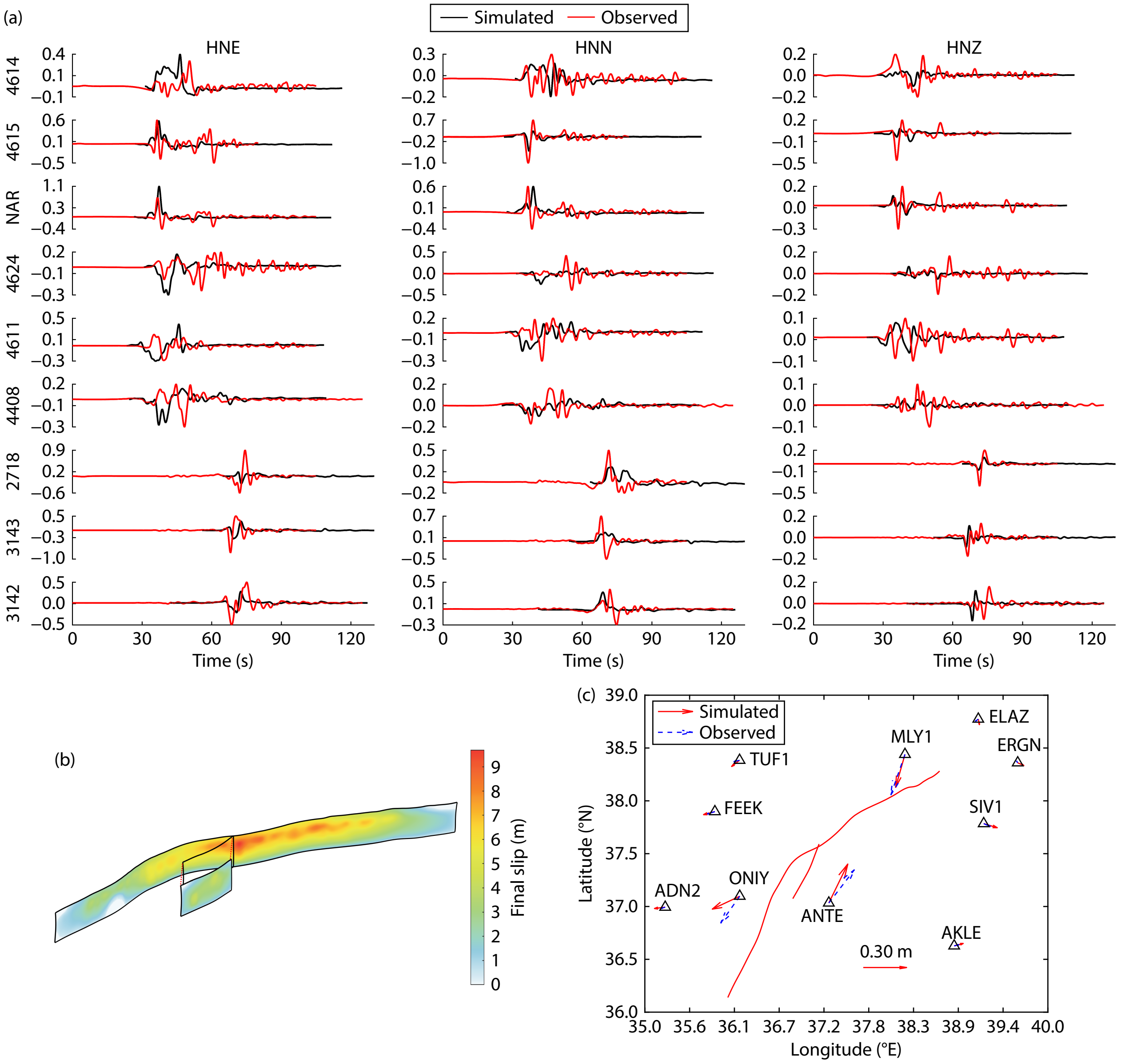

Figure S2. (a) Comparison of simulated velocity waveforms and recorded velocity waveforms at different stations; (b) final slip distribution on the fault plane; (c) comparison between simulated and observed surface GPS displacements.

triggering during the 2023 earthquake doublet in southeastern Türkiye. *Nat. Commun.*, *14*(1), 5564. https://doi.org/10.1038/s41467-023-41404-5

Lyberis, N., Yurur, T., Chorowicz, J., Kasapoglu, E., and Gundogdu, N. (1992). The East Anatolian Fault: An oblique collisional belt. *Tectonophysics*, *204*(1–2), 1–15. https://doi.org/10.1016/0040-1951(92)90265-8

Mai, P. M., Aspiotis, T., Aquib, T. A., Cano, E. V., Castro-Cruz, D., Espindola-Carmona, A., Li, B., Li, X., Liu, J. H., … Jónsson, S. (2023). The destructive earthquake doublet of 6 February 2023 in South-Central Türkiye and Northwestern Syria: Initial observations and analyses. *Seismic Record*, *3*(2), 105–115. https://doi.org/10.1785/0320230007

Meade, B. J. (2007). Algorithms for the calculation of exact displacements, strains, and stresses for triangular dislocation elements in a uniform elastic half space. *Comput. Geosci.*, *33*(8), 1064–1075. https://doi.org/10.1016/j.cageo.2006.12.003

Melgar, D., Taymaz, T., Ganas, A., Crowell, B. W., Öcalan, T., Kahraman, M., Tsironi, V., Yolsal-Çevikbilen, S., Valkaniotis, S., … Altuntas, C. (2023). Sub- and super-shear ruptures during the 2023 Mw 7.8 and Mw 7.6 earthquake doublet in SE Türkiye. *Seismica*, *2*(3), 1–10. https://doi.org/10.26443/seismica.v2i3.387

Nikkhoo, M., and Walter, T. R. (2015). Triangular dislocation: An analytical, artefact-free solution. *Geophys. J. Int.*, *201*(2), 1119–1141. https://doi.org/10.1093/gji/ggv035

Okada, Y. (1985). Surface deformation due to shear and tensile faults in a half-space. *Bull. Seismol. Soc. Am.*, *75*(4), 1135–1154. https://doi.org/10.1785/BSSA0750041135

Okada, Y. (1992). Internal deformation due to shear and tensile faults in a half-space. *Bull. Seismol. Soc. Am.*, *82*(2), 1018–1040. https://doi.org/10.1785/BSSA0820021018

Okuwaki, R., Yagi, Y., Taymaz, T., and Hicks, S. P. (2023). Multi-scale rupture growth with alternating directions in a complex fault network during the 2023 south-eastern Türkiye and Syria earthquake doublet. *Geophys. Res. Lett.*, *50*(12), e2023GL103480. https://doi.org/10.1029/2023GL103480

Ramos, M. D., Huang, Y. H., Ulrich, T., Li, D., Gabriel, A. A., and Thomas, A. M. (2021). Assessing margin-wide rupture behaviors along the Cascadia megathrust with 3-D dynamic rupture simulations. *J. Geophys. Res.: Solid Earth*, *126*(7), e2021JB022005. https://doi.org/10.1029/2021JB022005

Reilinger, R., McClusky, S., Vernant, P., Lawrence, S., Ergintav, S., Cakmak, R., Ozener, H., Kadirov, F., Guliev, I., … Karam, G. (2006). GPS constraints on continental deformation in the Africa–Arabia–Eurasia continental collision zone and implications for the dynamics of plate interactions. *J. Geophys. Res.: Solid Earth*, *111*(B5), B05411. https://doi.org/10.1029/2005JB004051

Reitman, N. G., Briggs, R. W., Barnhart, W. D., Thompson Jobe, J. A., DuRoss, C. B., Hatem, A. E., Gold, R. D., Akçiz, S., Koehler, R. D., … Collett, C. (2023). Fault rupture mapping of the 6 February 2023 Kahramanmaraş, Türkiye, earthquake sequence from satellite data (ver. 1.1, February 2024). Reston, Virginia: U.S. Geological Survey. https://doi.org/10.5066/P985I7U2

Ren, C. M., Wang, Z. X., Taymaz, T., Hu, N., Luo, H., Zhao, Z. Y., Yue, H., Song, X. D., Shen, Z. K., … Ding, H. Y. (2024). Supershear triggering and cascading fault ruptures of the 2023 Kahramanmaraş, Türkiye, earthquake doublet. *Science*, *383*(6680), 305–311. https://doi.org/10.1126/science.adi1519

Rosakis, A., Abdelmeguid, M., and Elbanna, A. (2023). Evidence of early supershear transition in the Feb 6th 2023 M_w 7.8 Kahramanmaraş Turkey earthquake from near-field records. *EarthArXiv*. https://doi.org/10.31223/X5W95G

Tan, O., and Taymaz, T. (2006). Active tectonics of the Caucasus: Earthquake source mechanisms and rupture histories obtained from inversion of teleseismic body waveforms. In Y. Dilek, et al. (Eds.), *Postcollisional Tectonics and Magmatism in the Mediterranean Region and Asia* (pp. 531–578). Boulder, Colorado: Geological Society of America. https://doi.org/10.1130/2006.2409(25)

Taymaz, T., Eyidoǧan, H., and Jackson, J. (1991). Source parameters of large earthquakes in the East Anatolian Fault Zone (Turkey). *Geophys. J. Int.*, *106*(3), 537–550. https://doi.org/10.1111/j.1365-246X.1991.tb06328.x

Taymaz, T., Ganas, A., Yolsal-Çevikbilen, S., Vera, F., Eken, T., Erman, C., Keleş, D., Kapetanidis, V., Valkaniotis, S., … Öcalan, T. (2021). Source mechanism and rupture process of the 24 January 2020 *Mw 6.7* Doğanyol-Sivrice earthquake obtained from seismological waveform analysis and space geodetic observations on the East Anatolian Fault Zone (Turkey). *Tectonophysics*, *804*, 228745. https://doi.org/10.1016/j.tecto.2021.228745

Wang, Z., Fu, Y., and Pei, S. P. (2024). Relationship between seismic structures and the diverse rupture processes of the 2023 Türkiye earthquake doublet. *Sci. China Earth Sci.*, *67*(9), 2810–2823. https://doi.org/10.1007/s11430-023-1324-y

Wang, Z. J., Zhang, W. Q., Taymaz, T., He, Z. Q., Xu, T. H., and Zhang, Z. G. (2023). Dynamic rupture process of the 2023 *Mw* 7.8 Kahramanmaraş earthquake (SE Türkiye): Variable rupture speed and implications for seismic hazard. *Geophys. Res. Lett.*, *50*(15), e2023GL104787. https://doi.org/10.1029/2023GL104787

Xi, X., Li, C. L., Li, T., Wei, Z. Y., Ma, Z. F., Zhang, G. H., Qu, C. Y., He, H. L., and Shan, X. J. (2025). Fault geometry and rupture speed as controls on off-fault deformation in the 2023 Turkey-Syria earthquakes. *Commun. Earth Environ.*, *6*(1), 103. https://doi.org/10.1038/s43247-025-02089-4

Yao, S. L., and Yang, H. F. (2025). Rupture phases reveal geometry-related rupture propagation in a natural earthquake. *Sci. Adv.*, *11*(4), eadq0154. https://doi.org/10.1126/sciadv.adq0154

Yilmaz, H., Over, S., and Ozden, S. (2006). Kinematics of the East Anatolian Fault Zone between Turkoglu (Kahramanmaras) and Celikhan (Adiyaman), eastern Turkey. *Earth Planets Space*, *58*(11), 1463–1473. https://doi.org/10.1186/BF03352645

Zhang, W. Q., Liu, Y. J., and Chen, X. F. (2023). A mixed-flux-based nodal discontinuous Galerkin method for 3D dynamic rupture modeling. *J. Geophys. Res.: Solid Earth*, *128*(6), e2022JB025817. https://doi.org/10.1029/2022JB025817

Zhang, Y. J., Tang, X. W., Liu, D. C., Taymaz, T., Eken, T., Guo, R. M., Zheng, Y., Wang, J. Q., and Sun, H. P. (2023). Geometric controls on cascading rupture of the 2023 Kahramanmaraş earthquake doublet. *Nat. Geosci.*, *16*(11), 1054–1060. https://doi.org/10.1038/s41561-023-01283-3